Journal of Electronics and Electrical Engineering
https://ojs.wiserpub.com/index.php/JEEE/

Article

DC and RF Performance of an N-channel Monolayer Black Phosphorus Nanoribbon Transistor

Khairul Alam

Department of Electrical and Electronic Engineering, East West University, Dhaka, Bangladesh
E-mail: kalam@ewubd.edu

Received: 13 April 2023; **Revised:** 14 May 2023; **Accepted:** 22 May 2023

Abstract: Two-dimensional black phosphorus is a relatively new discovery. There are numerous studies on black phosphorus two-dimensional transistors that focus on analog and RF performance. However, the RF performance of black phosphorus nanoribbon transistors is yet to be explored. We use a four-band tight binding Hamiltonian in conjunction with a non-equilibrium Green's function quantum transport simulator to investigate both the DC and RF performance of a monolayer black phosphorus nanoribbon transistor. We found that electron intra-band tunneling is responsible for current flow in the off-state, while in the on-state, the electrons flow over the top of the channel barrier potential. With a V_{DD} of 0.4 volt and a gate length of 5 nm, our black phosphorus nanoribbon transistor has DC performance metrics of 510 μA/μm on-state current, 10^5 on/off current ratio, and 65 mV/dec inverse subthreshold slope. The device's RF performance characteristics are as follows: cut-off (unity current gain) frequency of 772.84 GHz, maximum oscillation (unity power gain) frequency of 1.15 THz, and open circuit voltage gain of 26.7 dB with transistor operating in the on-state. The RF performance of the device is found to be significantly impacted by the source and drain contact resistances. With source and drain resistances set to zero, the cut-off frequency increases to 995.23 GHz and the unity power gain frequency increases to 4.16 THz. The device shows unconditional stability above 893 GHz and it is conditionally stable below this frequency.

Keywords: DC performance, RF performance, black phosphorus, nanoribbon transistor, NEGF, tight binding

1. Introduction

Due to their unique electrical, mechanical, and thermal properties, two-dimensional (2D) materials have garnered considerable interest in the scientific community [1–4]. Even at the short channel limits, the 2D field-effect transistors (FETs) show great mobility, high on/off current ratio, and minimal leakage [5–9]. Graphene [5,8,9] and transition metal dichalcogenides (TMDs) [7] are two of the most investigated materials on the extensive list of 2D candidates. However, graphene has a zero band gap, and the poor mobility of TMDs restricts their usefulness [10]. Black phosphorus (BP) is a new and promising addition to the list. Its puckered shape and layer-dependent direct band gap, which varies from ~0.35 eV (bulk) to ~1.85 eV (monolayer) [11], make it an interesting material to study. This material also possesses notable in-plane anisotropic properties [12,13].

Because of its high mobility, controlled band gap, and anisotropic band structure, BP is an excellent option for use in electronic as well as optoelectronic applications [12]. On BP 2D FETs, a significant amount of research has been done [14–21]. It has been said that the performance of BP transistors can be higher than that of their MoS_2 equivalents [16]. Applications of BP as radio-frequency (RF) transistors have also been investigated alongside nanotransistors [19,22–28]. Theoretically estimated high RF figures of merit have a unity

DOI: https://doi.org/10.37256/jeee.2120232835

power gain frequency of f_{max} = 950 GHz [27]. Experiments have shown that a device with a channel length of 300 nm can achieve a f_{max} of 20 GHz [22].

Despite substantial research on 2D BP FETs, one-dimensional (1D) black phosphorus nanoribbons (NRs) and nanotubes (NTs) have received less attention [29–34]. Both experiments and theoretical first-principles simulations have been used to investigate the structural [29] and thermal [35,36] stability, band gap fluctuation [37], and characterization [38] of 1D BP NRs. Feng et al. [30] experimentally showed complementary BP NR top gate FETs. According to their findings, the BP NR 1D FETs outperform the BP 2D FETs by an order of magnitude in terms of on-state current, five times in terms of subthreshold slope, and four times in terms of peak transconductance. However, we realize that the RF performance of BP 1D FETs is yet to be explored.

This study uses an in-house developed quantum transport code and a four-band tight binding Hamiltonian to theoretically investigate the DC and RF performance of a monolayer 5 nm gate length BP NR transistor. The transistor exhibits a high on/off current ratio with an inverse subthreshold slope of 65 mV/dec when operated at a DC bias. In the off-state, electron intra-band tunneling regulates the current flow, and in the on-state, thermionic emission over the channel potential barrier does the same. An equivalent circuit is utilized in order to assess the radio-frequency performance. The parameters of the circuit are established by the use of numerical simulation. The RF performance parameters calculated are as follows: a unity current gain frequency of 772.84 GHz, a unity power gain frequency of 1.15 THz, and an open circuit voltage gain of 26.7 dB.

2. Device Structure and Simulation Approach

With gate length L_G = 5 nm, effective oxide thickness EOT = 0.45 nm, and V_{DD} = 0.4 V, which are near the specifications of 2027 low-power logic [39], we simulate a double-gate monolayer BP NR 1D FET. t_{ox} = 2.15 nm and ε_{ox} = 19 represent the physical oxide thickness and dielectric constant, respectively, that we employ in our simulation. Figure 1 depicts the cross-section of the device. The lengths of the source and drain extensions, L_S and L_D, are both set to 10 nm. Both the source and the drain are doped with a donor concentration of N_D = 1.25×10^{13} cm^{-2}, making the channel intrinsic. In order to align the source conduction band with the source Fermi level, we selected this doping density.

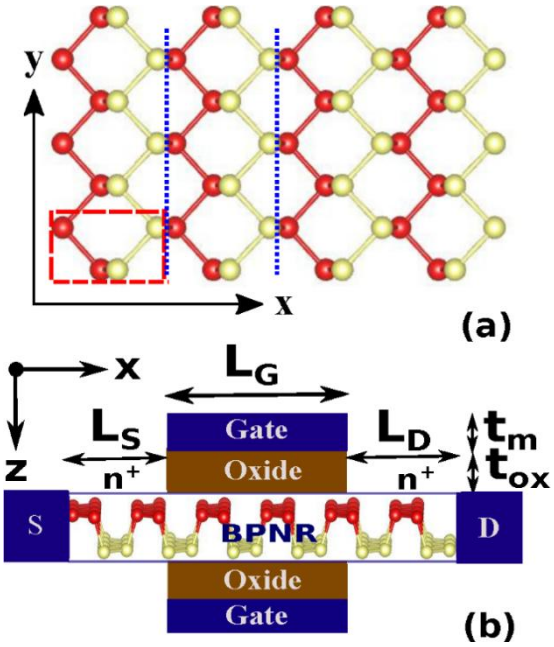

Figure 1. (a) Monolayer BP nanoribbon. x and y axes represent the armchair and the zigzag directions, respectively. The red rectangle shows the 4 atoms unit cell, and the vertical blue lines show the nanoribbon unit cell used in recursive Green's function calculation. (b) The two-dimensional cross-section of $x - z$ plane of the BP NR 1D FET used in this study.

A four-band tight binding Hamiltonian is used to model BP [11]

$$H = \sum_{i \neq j} t_{ij}^{\|} c_i^{+} c_j \tag{1}$$

In this equation, i and j refer to the lattice sites, $t_{ij}^{\|}$ is the in-layer hopping parameter between sites i and j, and c_i^+ and c_j are the operators for creating and destroying electrons at sites i and j, respectively. Note that the on-site energies have been set to zero. The model has been validated against the *ab initio* self-consistent GW_0 results [11]. The red rectangle in Figure 1(a) represents the four atoms that make up the BP monolayer's unit cell. Our recursive Green's function algorithm [34,40,41] uses nanoribbon unit cell depicted by the blue vertical lines in Figure 1(a). The layer (or unit cell) Hamiltonian h_L and the layer-to-layer (or unit cell-to-unit cell) coupling matrices $h_{L,L+1}$ and $h_{L,L-1}$ have sizes that are 4 times the number of unit cells along the y (zigzag) direction. h_L and $h_{L,L+1}$ can be written as [42]

$$h_L = \begin{bmatrix} \alpha_u & \beta_{uW} & \beta_{uWF} & 0 & 0 \\ \beta_{uW}^\dagger & \alpha_u & \beta_{uW} & \beta_{uWF} & 0 \\ \beta_{uWF}^\dagger & \beta_{uW}^\dagger & \alpha_u & \beta_{uW} & \ddots \\ 0 & \beta_{uWF}^\dagger & \beta_{uW}^\dagger & \alpha_u & \ddots \\ 0 & 0 & \ddots & \ddots & \ddots \end{bmatrix} \tag{2}$$

$$h_{L,L+1} = \begin{bmatrix} \beta_{uL} & \beta_{uLF} & 0 & 0 & 0 \\ \beta_{uLB} & \beta_{uL} & \beta_{uLF} & 0 & 0 \\ 0 & \beta_{uLB} & \beta_{uL} & \beta_{uLF} & \ddots \\ 0 & 0 & \beta_{uLB} & \beta_{uL} & \ddots \\ 0 & 0 & 0 & \ddots & \ddots \end{bmatrix}, \tag{3}$$

and $h_{L,L-1} = h_{L,L+1}^\dagger$. The block matrices α_u, β_{uW}, β_{uWF}, β_{uL}, β_{uLF} and β_{uLB} are 4 × 4 matrices, and are provided in Ref. [42]'s Eqs. (2–5). There in Table 1, the hopping parameters are also provided.

We have the required three matrices, h_L, $h_{L,L+1}$ and $h_{L,L-1}$ in hand. We can now apply the recursive Green's function approach to determine the electron density from the diagonal portions of the source and drain spectral functions [34,40,41],

$$n_L(x,y,z) = \frac{1}{\delta\Omega}\int \frac{dE}{2\pi} diag\left[A_{L,L}^S(E,x,y,z) f(E,\mu_S) + A_{L,L}^D(E,x,y,z) f(E,\mu_D)\right]. \tag{4}$$

In this equation, $\delta\Omega$, f and μ_S stand for grid volume, Fermi distribution function, and Fermi energy levels at the source and drain, respectively. The spectral functions are given by $A_{L,L}^S = G_{L,1}\Gamma_{1,1}G_{1,L}^\dagger$, and $A_{L,L}^D = i\left(G_{L,L} - G_{L,L}^\dagger\right) - A_{L,L}^S$, where the broadening function is supplied by $\Gamma_{1,1} = i\left(\Sigma_{1,1} - \Sigma_{1,1}^\dagger\right)$ and the decimation method [43,44] is used to get the boundary self-energy $\Sigma_{1,1} = h_{1,0}g_{0,0}h_{0,1}$. The required blocks of full Green's function are determined by sequentially solving the following equations.

$$\begin{aligned} g_{L,L} &= \left(E - h_L - U_L - h_{L,L+1}g_{L+1,L+1}h_{L+1,L}\right)^{-1} \\ G_{1,1} &= \left(E - h_1 - U_1 - \Sigma_{1,1} - h_{1,2}g_{2,2}h_{2,1}\right)^{-1} \\ G_{L,L} &= g_{L,L} + g_{L,L}h_{L,L-1}G_{L-1,L-1}h_{L-1,L}g_{L,L} \\ G_{L,1} &= g_{L,L}h_{L,L-1}G_{L-1,1} \end{aligned} \tag{5}$$

Poisson's solver is used to calculate the layer's potential energy, U_L. The recursive calculation starts from the right contact with $L = N$ and $\Sigma_{N,N} = h_{N,N+1}g_{N+1,N+1}h_{N+1,N}$.

Potential profile is obtained by solving a three-dimensional Poisson's equation in Cartesian coordinates

$$\frac{\partial}{\partial x}\left(\varepsilon\frac{\partial V}{\partial x}\right) + \frac{\partial}{\partial y}\left(\varepsilon\frac{\partial V}{\partial y}\right) + \frac{\partial}{\partial z}\left(\varepsilon\frac{\partial V}{\partial z}\right) = -\rho. \tag{6}$$

The potential profile and location dependent dielectric constant are represented by V ($U=-qV$) and ε, respectively. $\rho=(N_D-n)$ is the charge density. To solve the Poisson's equation, a finite difference discretization with Newton-Rapshon approach is utilized. At the gate metal, potential is maintained constant, while all other boundaries have their normal electric field component set to zero. We use a contact resistance value of $R_S+R_D=130\ \Omega\cdot\mu$m [34]. Experimentally, it has been possible to attain a contact resistance value for BP FETs of 135 $\Omega\cdot\mu$m with a Ni contact [45] and 310 $\Omega\cdot\mu$m with a Ti contact [46]. Theoretically, a ceiling of 14 $\Omega\cdot\mu$m has been expected [47]. The contact resistance used in this work is thus not too far from becoming achievable.

The first step in the self-consistent loop is to make an educated guess about the potential profile. After that, we compute the charge density, Eq. 4, as well as the current [40,41]

$$I_D=\frac{q}{\hbar}\int\frac{dE}{2\pi}\mathrm{tr}\left(\Gamma_{1,1}\left[\mathrm{A}_{1,1}-G_{1,1}\Gamma_{1,1}G_{1,1}^{\dagger}\right]\right)\left(f_S-f_D\right). \tag{7}$$

The intrinsic component of the device potential is updated using the computed current in the following way: $V_{GS}^{i}=V_{GS}-I_DR_S$ and $V_{DS}^{i}=V_{DS}-I_D\left(R_S+R_D\right)$. These newly calculated voltages serve as the boundary condition when Poisson's equation is solved using the data from the most recent computation of charge density. The loop remains active until convergence is reached. Anderson mixing [48] is used to hasten the convergence. After the loop has reached convergence, the results are saved, and then we move on to calculating the next bias value. The simulation software is developed internally using open-source Julia programming language [49].

3. Simulation Results and Discussions

Figure 2 depicts the E-k dispersions of monolayer BP nanoribbon with a width of W = 2.3 nm that we used in our simulation. The energy reference is located in the band gap's midpoint. Seven 4-atom unit cells (Figure 1), or 28 atoms, make up the nanoribbon unit cell. The transport route is in the armchair direction (x in Fig. 1), whereas the quantization direction (nanoribbon width) is along the zigzag direction (y in Figure 1). The nanoribbon has a 1.918 eV direct band gap. The top valence subbands merge as a result of a significantly heavier hole in the quantization (zigzag) direction [18], but the bottom conduction subbands are closely spaced.

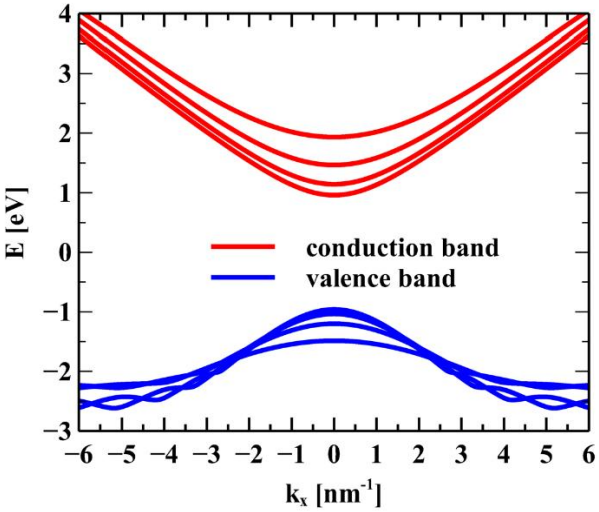

Figure 2. A few bands of monolayer BP NR. The width of the nanoribbon W = 2.3 nm. k_x is along the ribbon armchair direction. Energy is zero at the center of the band gap.

Figure 3 displays the simulated $I-V$ characteristics of an n-channel double gate nanoribbon field-effect transistor. The I_D-V_D characteristic is similar to that of a standard MOSFET. In order to get the I_D-V_G characteristics, we began by setting the drain bias at 0.4 volts and then sweep the gate bias across a broad range. The off-state current is then adjusted by shifting the I_D-V_G characteristics to a value of $5\times10^{-3}\ \mu\mathrm{A}/\mu$m when

the gate bias is at zero. The calculated current is in μA. Therefore, in order to obtain the current measured in $\mu A/\mu m$, we divided it by the width of the nanoribbon. The device features a 65 mV/dec subthreshold slope, a 510 $\mu A/\mu m$ on-state current, and a 1.02×10^5 on/off current ratio. Experiments have shown that an optimized few-layer BP 2D FET doped with lithium has a high on-state current of 773 $\mu A/\mu m$ and an on/off current ratio of 7.2×10^5 [17]. It is important to note that these values were determined by conducting measurements at a low temperature of 20^0 K for a device that had a long channel and a gate bias of −4 volts.

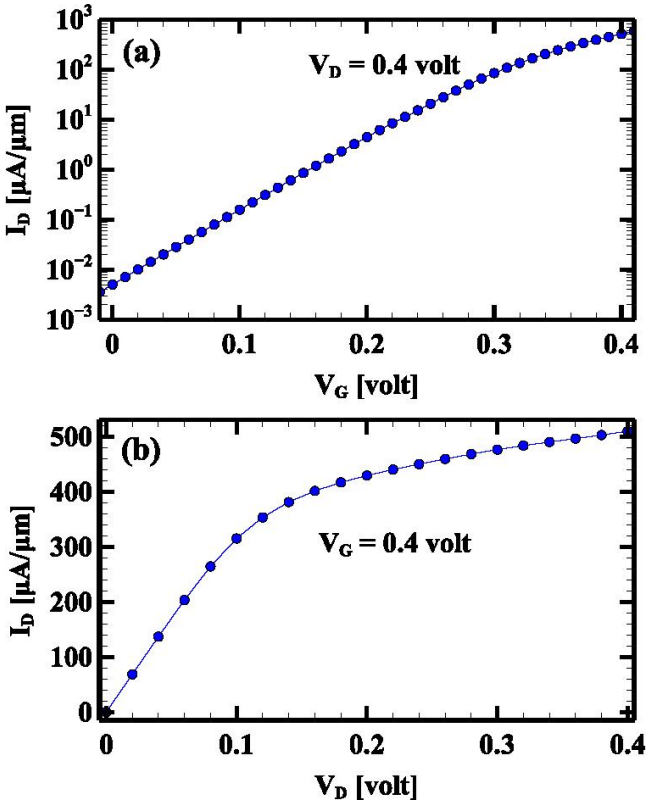

Figure 3. (a) nFET I_D - V_G characteristics at V_D = 0.4 V. V_G = 0 represents the off-state, while V_G = 0.4 volt represents the on-state. (b) I_D - V_D characteristics at V_G = 0.4 volt.

In order to acquire a better understanding of electron transport, we depict the energy profile of current, denoted by J_E, overlaid on the conduction band profile in Figure 4(a) at a gate bias of 0.31 volt. The Fermi level at the source is used as the zero energy reference. The dashed line indicates that the top of the conduction band is located at 0.063 eV. This value represents the barrier energy for electrons that are injected from the source contact. Any injected electrons with energies lower than this barrier energy will be able to "tunnel" through it and reach the drain terminal. This tunneling current can be determined by integrating J_E from −0.4 to 0.063 eV (barrier top), which accounts for 49.5% of the total current when the gate bias is 0.31 volt. In the remaining 50.5% of the total current, known as the thermal current, electrons pass over the barrier top. The current is broken down into its tunneling component and its thermal component across the entire voltage range in Figure 4(b). Clearly, electron tunneling dominates in low bias, whereas thermionic emission predominates at higher biases. Current in the off-state is 83% tunneling, while current in the on-state is 74% thermionic.

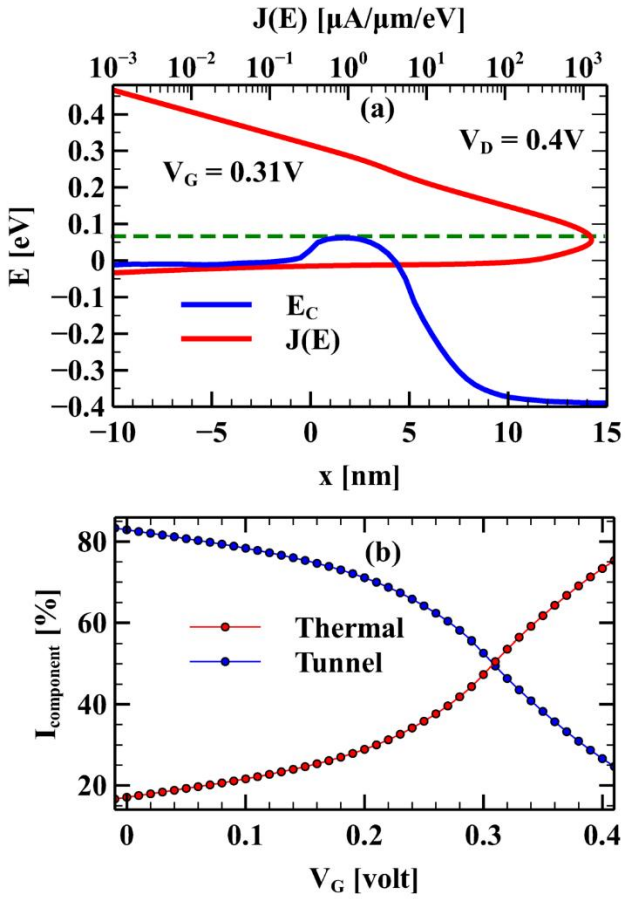

Figure 4. Current energy density, labeled by J_E, is plotted over the conduction band profile, labeled by E_C, at $V_G = 0.31$ volt. The conduction band top located at 0.063 eV is depicted by a dashed horizontal line. Source Fermi level is set to have zero energy.

After having determined the DC figures of merit (on-state current, inverse subthreshold slope, and on-off current ratio) and having gained an understanding of the mechanism underlying electron transport, we moved on to evaluating the device's RF performance parameters. In order to accomplish this, we will be looking at the small signal equivalent circuit that is depicted in Figure 5. The following is how we determine the transconductance, denoted by g_m, and the output conductance, denoted by g_0.

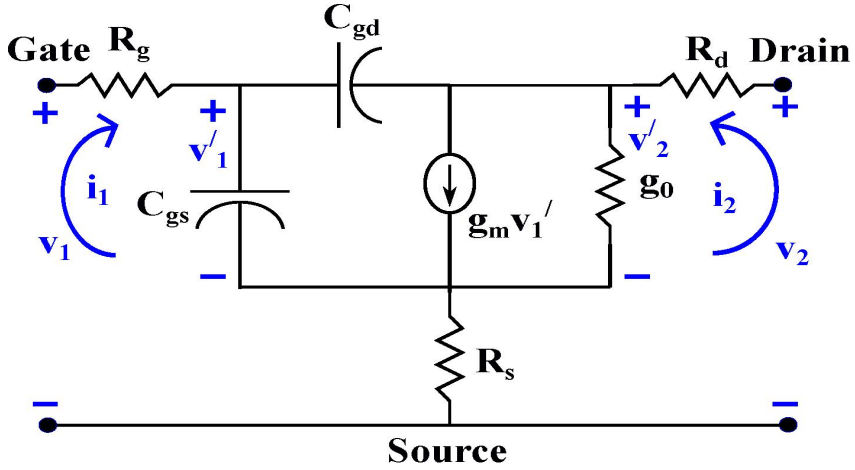

Figure 5. Equivalent small signal circuit of the simulated NR FET for RF performance analysis.

$$g_m = \frac{\partial I_D}{\partial V_{GS}}\Big|V_{DS}$$
$$g_0 = \frac{\partial I_D}{\partial V_{DS}}\Big|V_{GS} \tag{8}$$

For g_m calculation, we set V_{DS} to 0.4 volt and sweep V_{GS} from 0 to 0.4 volt. Similarly, V_{GS} is set to 0.4 volt and V_{DS} is swept from 0 to 0.4 volt to calculate g_0. The computed conductances are shown in Figure 6. Transconductance g_m is a figure of merit that determines the amplification delivered by a transistor. It increases with gate bias, and its value in on-state is 6.7 mS/μm. In linear region g_0 is large due to uniform channel, and it decreases with drain bias due to channel length modulation. In on-state $g_0 = 0.31$ mS/μm, that is, the output resistance is $r_0 = 1/g_0 = 3.2\ k\Omega/\mu$m.

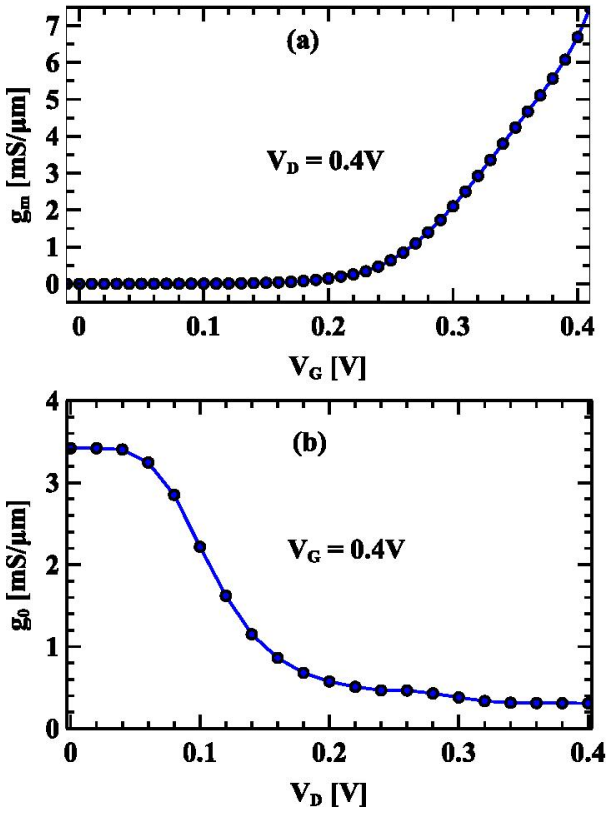

Figure 6. (a) Transconductance g_m vs V_G at V_D = 0.4 volt. (b) Output conductance g_0 vs V_D at V_G = 0.4 volt.

The capacitances from the gate to the source and from the gate to the drain can be estimated as follows

$$C_{gs} = \frac{2C_{ox}C_{qs}}{2C_{ox}+C_{qs}}$$
$$C_{gd} = \frac{2C_{ox}C_{qd}}{2C_{ox}+C_{qd}}. \tag{9}$$

$C_{ox} = \varepsilon_{ox}/t_{ox}$ represents the oxide capacitance per unit area, and the factor 2 compensates for two identical gates [50]. The quantum capacitances, C_{qs} and C_{qd}, are computed as

$$C_{qs} = \frac{\partial Q_{ch}}{\partial \Psi_s}$$
$$C_{qd} = \frac{\partial Q_{ch}}{\partial (\Psi_s - V_D)} \tag{10}$$

where Q_{ch} refers to the channel charge and Ψ_s refers to the surface potential. Figure 7 shows the computed capacitances, C_{gs} and C_{gd}. These capacitances play crucial roles for analyzing RF performance, such as the cutoff frequency, f_T and the maximum oscillation frequency, $f_{\max}$.

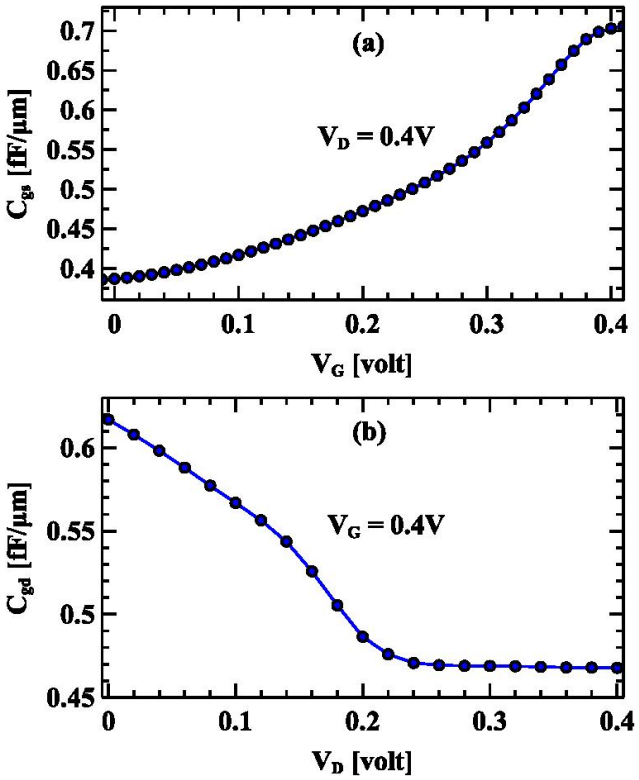

Figure 7. (a) Gate to source capacitance C_{gs} vs V_G at V_D = 0.4 volt. (b) Gate to drain capacitance C_{gd} vs V_D at V_G = 0.4 volt.

To determine the RF performance metrics, we first derive the admittance matrix of the intrinsic part of the equivalent circuit, Figure 5, as follows

$$\begin{bmatrix} i_1 \\ i_2 \end{bmatrix} = \begin{bmatrix} jw(C_{gs}+C_{gd}) & -jwC_{gd} \\ g_m - jwC_{gd} & g_0 + jwC_{gd} \end{bmatrix} \begin{bmatrix} v_1' \\ v_2' \end{bmatrix} = [Y'] \begin{bmatrix} v_1' \\ v_2' \end{bmatrix}. \tag{11}$$

Now the voltage relation between extrinsic part (including R_g, R_s and R_d) and intrinsic part can be written as

$$\begin{aligned} \begin{bmatrix} v_1 \\ v_2 \end{bmatrix} &= \begin{bmatrix} v_1' \\ v_2' \end{bmatrix} + \begin{bmatrix} R_s + R_g & R_s \\ R_s & R_s + R_d \end{bmatrix} \begin{bmatrix} i_1 \\ i_2 \end{bmatrix} \\ &= [Y']^{-1} \begin{bmatrix} i_1 \\ i_2 \end{bmatrix} + \begin{bmatrix} R_s + R_g & R_s \\ R_s & R_s + R_d \end{bmatrix} \begin{bmatrix} i_1 \\ i_2 \end{bmatrix}. \end{aligned} \tag{12}$$

That is, the admittance matrix of the full equivalent circuit is

$$Y = \left[[Y']^{-1} + \begin{bmatrix} R_s + R_g & R_s \\ R_s & R_s + R_d \end{bmatrix} \right]^{-1} \tag{13}$$

From the admittance matrix, we can calculate the short circuit current gain, $A_i = Y_{21} / Y_{11}$, open circuit voltage gain, $A_v = -Y_{21} / Y_{22}$, and the unilateral power gain [51] as

$$U = \frac{|Y_{21} - Y_{12}|^2}{4\left[\mathrm{Re}(Y_{11})\mathrm{Re}(Y_{22}) - \mathrm{Re}(Y_{12})\mathrm{Re}(Y_{21})\right]}. \tag{14}$$

The voltage gain at DC can be written as $A_v(f \to 0) = g_m/g_0$ [52]. After substitution of g_m and g_0 in on-state we get $A_v(0) = 26.7$ dB. Figure 8 depicts the on-state short circuit current gain and the on-state unilateral power gain. In the calculations, we use $R_s = R_d = 65\ \Omega \cdot \mu$m [34] and $R_g = 4.4\ \Omega \cdot \mu$m [51,53]. The plot allows us to determine that the cut-off frequency, also known as the unity current gain frequency (0 dB), is equal to $f_T = 772.84$ GHz. In a similar vein, the frequency at which the power gain is equal to one, also known as the highest oscillation frequency, is equal to $f_{\max} = 1.12$ THz. For the nanoribbon FET, the source and drain contact resistances have significant effects on f_T and $f_{\max}$. If we set the contact resistances, R_s and R_d, to zero then f_T can be analytically derived as [52].

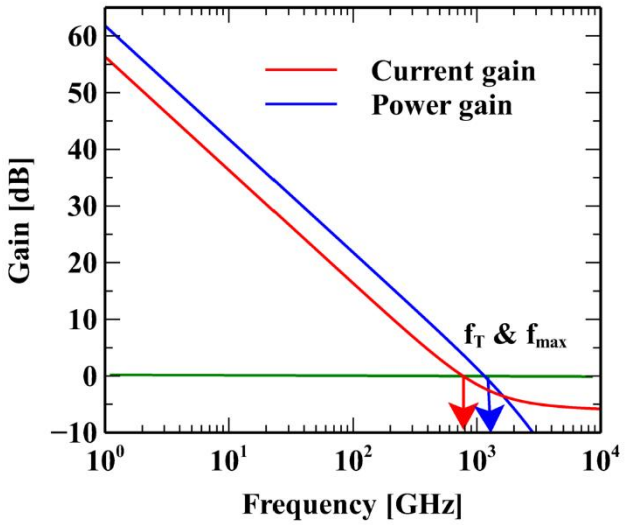

Figure 8. Plots of unilateral power gain and short circuit current gain against frequency in the on-state.

$$f_T = \frac{g_m}{2\pi\sqrt{C_{gs}^2 + 2C_{gs}C_{gd}}}, \tag{15}$$

and its value becomes $f_T = 995.23$ GHz. Under this condition, $f_{\max}$ can be analytically approximated as [25,53]

$$f_{\max} = \frac{f_T}{2\sqrt{g_0 R_g + 2\pi f_T C_{gd} R_g}}, \tag{16}$$

and its value becomes 4.16 THz. Clearly, the contact resistances have significant effects on f_T and $f_{\max}$, of which, $f_{\max}$ is primarily affected. In our NR FET, we see that $f_{\max} > f_T$. That means the current is saturated with increasing drain bias and this results in smaller g_0. The opposite relation is confirmed in graphene FET [54], that is, $f_{\max} < f_T$ due to semimetalic nature of graphene. So, BP NR FET is an attractive candidate for high frequency electronics.

Finally, we look into the stability issue of our nanoribbon FET. For this purpose, we calculate the stability factor *K* as follows [51]

$$K = \frac{2\,\mathrm{Re}(Y_{11})\,\mathrm{Re}(Y_{22}) - \mathrm{Re}(Y_{12}Y_{21})}{|Y_{12}Y_{21}|}. \tag{17}$$

since the components of the admittance matrix are a function of frequency, so is the stability factor. Figure 9 is a frequency-dependent plot of the stability factor. Stability ensures that passive loads connected to the input or output ports cannot accidentally induce oscillations in the network. To accomplish this, *K* must be greater than 1. The network is said to be conditionally stable if the value of *K* falls within the range −1< K<1, which means that it is stable when the source and load impedances are set up in certain ways. A *K* value below −1 makes the network unstable. From the results we see that the device is unconditionally stable above 893 GHz. That is, the

system will not show any oscillation above 893 GHz for any passive load at the input or output ports. Below 893 GHz operation, the network shows stable behavior for certain combinations of passive loads.

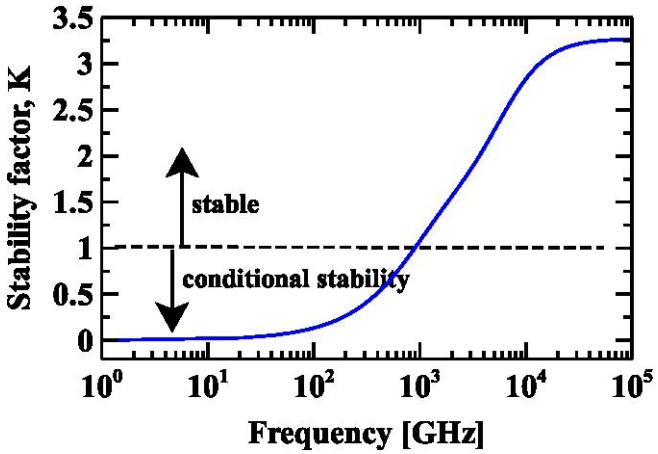

Figure 9. Stability factor *K* vs. frequency plot in on-state.

4. Conclusion

To summarize our findings, we used a four-band tight binding Hamiltonian and a non-equilibrium Green's function quantum transport code to investigate the transport mechanism and DC performance of a monolayer black phosphorus nanoribbon transistor. When in the off-state, electron transport is controlled by the intra-band tunneling, and when in the on-state, it is controlled by thermionic emission over the channel potential barrier. The device exhibits a current density of 510 μA/μm in its on state and a slope of 65 mV/dec in its subthreshold region, with an on/off current ratio of 10^5. Next, we use the admittance matrix of a two-port network with environmental influences to assess the device's RF performance. The gate-source terminals serve as the input port, while the drain-source terminals serve as the output port. With a maximum oscillation frequency of 1.15 THz, a cut-off frequency of 772.84 GHz, and an open-circuit voltage gain of 26.7 dB, this device boasts excellent RF performance metrics. The device is completely stable above 893 GHz and partially stable below that frequency.

Conflict of Interest

There is no conflict of interest for this study.

References

[1] Tan, C.; Cao, X.; Wu, Q.; Wu, X.; Yang, J.; Zhang, X.; Chen, J.; Zhao, W.; Han, S.; Nam, G.-H.; et al. Recent advances in ultrathin two-dimensional nanomaterials. *Chem. Rev.* **2017**, *117*, 6225–6331, https://doi.org/10.1021/acs.chemrev.6b00558.

[2] Robinson, J.A. Perspective: 2D for beyond CMOS. *APL Mater.* **2018**, *6*, 058202, https://doi.org/10.1063/1.5022769.

[3] Sang, D.K.; Wen, B.; Gao, S.; Zeng, Y.; Meng, F.; Guo, Z.; Zhang, H. Electronic and Optical Properties of Two-Dimensional Tellurene: From First-Principles Calculations. *Nanomaterials* **2019**, *9*, 1075, https://doi.org/10.3390/nano9081075.

[4] Shi, Z.; Cao, R.; Khan, K.; Tareen, A.K.; Liu, X.; Liang, W.; Zhang, Y.; Ma, C.; Guo, Z.; Luo, X.; et al. Two-dimensional tellurium: Progress, challenges, and prospects. *Nano-Micro Lett.* **2020**, *12*, 99.

[5] Zoghi, M.; Goharrizi, A.Y.; Saremi, M. Band Gap Tuning of Armchair Graphene Nanoribbons by Using Antidotes. *J. Electron. Mater.* **2016**, *46*, 340–346, https://doi.org/10.1007/s11664-016-4940-4.

[6] Zhu, F.; Chen, W.; Xu, Y.; Gao, C.-L.; Guan, D.-D.; Liu, C.-H.; Qian, D.; Zhang, S.-C.; Jia, J.-F. Epitaxi al growth of two-dimensional stanene. *Nat. Mater.* **2015**, *14*, 1020–1025, https://doi.org/10.1038/nmat43 84.

[7] Radisavljevic, B.; Radenovic, A.; Brivio, J.; Giacometti, V.; Kis, A. Single-layer MoS2 transistors. *Nat. Nanotechnol.* **2011**, *6*, 147–150, https://doi.org/10.1038/nnano.2010.279.

[8] Goharrizi, A.Y.; Zoghi, M.; Saremi, M. Armchair Graphene Nanoribbon Resonant Tunneling Diodes Usi ng Antidote and BN Doping. *IEEE Trans. Electron Devices* **2016**, *63*, 3761–3768, https://doi.org/10.110 9/ted.2016.2586459.

[9] Saremi, M.; Saremi, M.; Niazi, H.; Goharrizi, A.Y. Modeling of lightly doped drain and source graphene nanoribbon field effect transistors. *Superlattices Microstruct.* **2013**, *60*, 67–72, https://doi.org/10.1016/j. spmi.2013.04.013.

[10] Li, W.; Zhang, G.; Guo, M.; Zhang, Y.-W. Strain-tunable electronic and transport properties of MoS2 nanotubes. *Nano Res.* **2014**, *7*, 518–527, https://doi.org/10.1007/s12274-014-0418-y.

[11] Rudenko, A.N.; Yuan, S.; Katsnelson, M.I. Toward a realistic description of multilayer black phosphorus: From GW approximation to large-scale tight-binding simulations. *Phys. Rev. B* **2015**, *92*, 085419.

[12] Xia, F.; Wang, H.; Jia, Y. Rediscovering black phosphorus as an anisotropic layered material for optoelectronics and electronics. *Nat. Commun.* **2014**, *5*, 4458, https://doi.org/10.1038/ncomms5458.

[13] Lee, M.; Ali, N.; Ali, F.; Watanabe, K.; Taniguchi, T.; Yoo, W.J. Ultrahigh Anisotropic Transport Properties of Black Phosphorus Field Effect Transistors Realized by Edge Contact. *Adv. Electron. Mater.* **2021**, *8*, 2100988, https://doi.org/10.1002/aelm.202100988.

[14] Lam, K.-T.; Dong, Z.; Guo, J. Performance Limits Projection of Black Phosphorous Field-Effect Transistors. *IEEE Electron Device Lett.* **2014**, *35*, 963–965, https://doi.org/10.1109/led.2014.2333368.

[15] Liu, F.; Wang, Y.; Liu, X.; Wang, J.; Guo, H. Ballistic Transport in Monolayer Black Phosphorus Transi stors. *IEEE Trans. Electron Devices* **2014**, *61*, 3871–3876, https://doi.org/10.1109/ted.2014.2353213.

[16] Szabo, A.; Rhyner, R.; Carrillo-Nunez, H.; Luisier, M. Phonon-limited performance of single-layer, single-gate black phosphorus n- and p-type field-effect transistors. In Proceedings of 2015 IEEE International Electron Devices Meeting (IEDM), Washington, DC, USA, 7–9 December 2015, https://doi.org/10.1109/iedm.2015.7409680.

[17] Gao, T.; Li, X.; Xiong, X.; Huang, M.; Li, T.; Wu, Y. Optimized Transport Properties in Lithium Doped Black Phosphorus Transistors. *IEEE Electron Device Lett.* **2018**, *39*, 769–772, https://doi.org/10.1109/le d.2018.2820841.

[18] Brahma, M.; Kabiraj, A.; Bescond, M.; Mahapatra, S. Phonon limited anisotropic quantum transport in phosphorene field effect transistors. *J. Appl. Phys.* **2019**, *126*, 114502, https://doi.org/10.1063/1.5109057.

[19] Das, B.; Mahapatra, S. A predictive model for high-frequency operation of two-dimensional transistors from first-principles. *J. Appl. Phys.* **2020**, *128*, 234502, https://doi.org/10.1063/5.0030633.

[20] Jiang, B.; Huang, H.; Chen, R.; Li, G.; Flandre, D.; Wan, D.; Chen, X.; Liu, X.; Ye, C.; Liao, L. Black phosphorus field effect transistors stable in harsh conditions via surface engineering. *Appl. Phys. Lett.* **2020**, *117*, 111602, https://doi.org/10.1063/5.0021335.

[21] Cheng, R.; Yin, L.; Hu, R.; Liu, H.; Wen, Y.; Liu, C.; He, J. Modulation of Negative Differential Resista nce in Black Phosphorus Transistors. *Adv. Mater.* **2021**, *33*, e2008329, https://doi.org/10.1002/adma.202 008329.

[22] Wang, H.; Wang, X.; Xia, F.; Wang, L.; Jiang, H.; Xia, Q.; Chin, M.L.; Dubey, M.; Han, S.-J. Black Pho sphorus Radio-Frequency Transistors. *Nano Lett.* **2014**, *14*, 6424–6429, https://doi.org/10.1021/nl502971 7.

[23] Zhu, W.; Park, S.; Yogeesh, M.N.; McNicholas, K.M.; Bank, S.R.; Akinwande, D. Black Phosphorus Flexible Thin Film Transistors at Gighertz Frequencies. *Nano Lett.* **2016**, *16*, 2301–2306, https://doi.org/10.1021/acs.nanolett.5b04768.

[24] Chowdhury, S.F.; Yogeesh, M.N.; Banerjee, S.K.; Akinwande, D. Black Phosphorous Thin-Film Transistor and RF Circuit Applications. *IEEE Electron Device Lett.* **2016**, *37*, 449–451, https://doi.org/10.1109/led.2016.2536102.

[25] Yin, D.; AlMutairi, A.; Yoon, Y. Assessment of High-Frequency Performance Limit of Black Phosphorus Field-Effect Transistors. *IEEE Trans. Electron Devices* **2017**, *64*, 2984–2991, https://doi.org/10.1109/ted.2017.2699969.

[26] Xiong, K.; Li, C.; Li, L.; Guo, Q.; Watanabe, K.; Taniguchi, T.; Madjar, A.; Xia, F.; Hwang, J.C.M. Black Phosphorus MOSFET for Future-Generation Thin-Film Electronics Capable of Microwave Operation. In Proceedings of 2019 IEEE MTT-S International Microwave Symposium (IMS), Boston, MA, USA, 2–7 June 2019, https://doi.org/10.1109/mwsym.2019.8701087.

[27] Rathinam, R.; Pon, A.; Carmel, S.; Bhattacharyya, A. Analysis of black phosphorus double gate MOSFET using hybrid method for analogue/RF application. *IET Circuits, Devices Syst.* **2020**, *14*, 1167–1172, https://doi.org/10.1049/iet-cds.2020.0092.

[28] Valdez-Sandoval, L.M.; Ramirez-Garcia, E.; Park, S.; Akinwande, D.; Jimenez, D.; Pacheco-Sanchez, A. A Small-Signal Description of Black-Phosphorus Transistor Technologies for High-Frequency Applicati ons. *IEEE Microw. Wirel. Components Lett.* **2021**, *31*, 1055–1058, https://doi.org/10.1109/lmwc.2021.30 86047.

[29] Cai, K.; Liu, L.; Shi, J.; Qin, Q.H. Winding a nanotube from black phosphorus nanoribbon onto a CNT at low temperature: A molecular dynamics study. *Mater. Des.* **2017**, *121*, 406–413, https://doi.org/10.1016/ j.matdes.2017.02.084.

[30] Feng, X.; Wang, L.; Huang, X.; Chen, L.; Ang, K.W. Complementary Black Phosphorus Nanoribbons Field-Effect Transistors and Circuits. *IEEE Trans. Electron Devices* **2018**, *65*, 4122–4128, https://doi.org/10.1109/ted.2018.2848235.

[31] Li, C.; Xie, Z.; Chen, Z.; Cheng, N.; Wang, J.; Zhu, G. Tunable Bandgap and Optical Properties of Black Phosphorene Nanotubes. *Materials* **2018**, *11*, 304, https://doi.org/10.3390/ma11020304.

[32] Feng, X.; Huang, X.; Chen, L.; Tan, W.C.; Wang, L.; Ang, K.-W. High Mobility Anisotropic Black Phos phorus Nanoribbon Field-Effect Transistor. *Adv. Funct. Mater.* **2018**, *28*, https://doi.org/10.1002/adfm.20 1801524.

[33] Hu, M.; Yang, Z.; Zhou, W.; Li, A.; Pan, J.; Ouyang, F. Field effect transistors based on phosphorene nanoribbon with selective edge-adsorption: A first-principles study. *Phys. E: Low-dimensional Syst. Nanostructures* **2018**, *98*, 60–65, https://doi.org/10.1016/j.physe.2017.12.027.

[34] Alam, K. Transport and performance study of double-walled black phosphorus nanotube transistors. *Semicond. Sci. Technol.* **2022**, *37*, 085003, https://doi.org/10.1088/1361-6641/ac773e.

[35] Cai, K.; Wan, J.; Wei, N.; Cai, H.; Qin, Q.-H. Thermal stability of a free nanotube from single-layer black phosphorus. *Nanotechnology* **2016**, *27*, 235703, https://doi.org/10.1088/0957-4484/27/23/235703.

[36] Cai, K.; Wan, J.; Wei, N.; Qin, Q.H. Strength and stability analysis of a single-walled black phosphorus tube under axial compression. *Nanotechnology* **2016**, *27*, 275701–275701, https://doi.org/10.1088/0957-4484/27/27/275701.

[37] Guo, H.; Lu, N.; Dai, J.; Wu, X.; Zeng, X.C. Phosphorene Nanoribbons, Phosphorus Nanotubes, and van der Waals Multilayers. *J. Phys. Chem. C* **2014**, *118*, 14051–14059, https://doi.org/10.1021/jp505257g.

[38] Watts, M.C. Production and characterisation of phosphorene nanoribbons. Ph.D. dissertation, University College London, London, England, 2020.

[39] International Technology Roadmap for Semiconductors. Available online: http://www.itrs2.net (accessed on 5 February 2023).

[40] Lake, R.; Klimeck, G.; Bowen, R.C.; Jovanovic, D. Single and multiband modeling of quantum electron transport through layered semiconductor devices. *J. Appl. Phys.* **1997**, *81*, 7845–7869, https://doi.org/10. 1063/1.365394.

[41] Alam, K.; Lake, R.K. Leakage and performance of zero-Schottky-barrier carbon nanotube transistors. *J. Appl. Phys.* **2005**, *98*, 064307, https://doi.org/10.1063/1.2060962.

[42] Sarvari, H.; Liu, C.; Ghayour, A.H.; Shenavar, P.; Chen, Z.; Ghayour, R. Atomistic quantum transport simulation of multilayer phosphorene nanoribbon field effect transistors. *Phys. E: Low-dimensional Syst. Nanostructures* **2017**, *91*, 161–168, https://doi.org/10.1016/j.physe.2017.04.015.

[43] López-Sancho, M.P.; Sancho, J.M.L.; Rubio, J. Highly convergent schemes for the calculation of bulk and surface Green functions. *J. Phys. F Met. Phys.* **1985**, *15*, 851, https://doi.org/10.1088/0305-4608/15/4/009.

[44] Galperin, M.; Toledo, S.; Nitzan, A. Numerical computation of tunneling fluxes. *J. Chem. Phys.* **2002**, *117*, 10817–10826, https://doi.org/10.1063/1.1522404.

[45] Haratipour, N.; Namgung, S.; Grassi, R.; Low, T.; Oh, S.-H.; Koester, S.J. High-Performance Black Phosphorus MOSFETs Using Crystal Orientation Control and Contact Engineering. *IEEE Electron Device Lett.* **2017**, *38*, 685–688, https://doi.org/10.1109/led.2017.2679117.

[46] Telesio, F.; Le Gal, G.; Serrano-Ruiz, M.; Prescimone, F.; Toffanin, S.; Peruzzini, M.; Heun, S. Ohmic contact engineering in few–layer black phosphorus: approaching the quantum limit. *Nanotechnology* **2020**, *31*, 334002, https://doi.org/10.1088/1361-6528/ab8cf4.

[47] Poljak, M.; Matić, M.; Župančić, T.; Zeljko, A. Lower Limits of Contact Resistance in Phosphorene Nanodevices with Edge Contacts. *Nanomaterials* **2022**, *12*, 656, https://doi.org/10.3390/nano12040656.

[48] Wang, H.; Wang, G.; Huang, Q.; Chang, S. Accelerated solution of Poisson-Schrodinger equations in na noscale devices by Anderson mixing scheme. *Micro Nano Lett.* **2009**, *4*, 122–127, https://doi.org/10.104 9/mnl.2009.0032.

[49] https://julialang.org (accessed on 18 January 2023).

[50] Ge, L.; Gamiz, F.; Workman, G.; Veeraraghavan, S. On the gate capacitance limits of nanoscale DG and FD SOI MOSFETs. *IEEE Trans. Electron Devices* **2006**, *53*, 753–758, https://doi.org/10.1109/ted.2006. 871412.

[51] Cantos, F.P. Modelling of field-effect transistors based on 2d materials targeting high-frequency applications. Ph.D. dissertation, Universitat Autonoma de Barcelona, Barcelona, Spain, 2017.

[52] Taur Y.; Ning, T.H. Fundamentals of Modern VLSI Devices, 3rd ed. Cambridge University Press: Cambridge, England, 2022.

[53] Xia, F.; Perebeinos, V.; Lin, Y.-M.; Wu, Y.; Avouris, P. The origins and limits of metal–graphene junction resistance. *Nat. Nanotechnol.* **2011**, *6*, 179–184, https://doi.org/10.1038/nnano.2011.6.

[54] Wu, Y.; Jenkins, K.A.; Valdes-Garcia, A.; Farmer, D.B.; Zhu, Y.; Bol, A.A.; Dimitrakopoulos, C.; Zhu, W.; Xia, F.; Avouris, P.; et al. State-of-the-Art Graphene High-Frequency Electronics. *Nano Lett.* **2012**, *12*, 3062–3067, https://doi.org/10.1021/nl300904k.